

1 **Predictive potential of Perzyna viscoplastic modelling**  
2 **for granular geomaterials**

3 **M. Lazari <sup>a,\*</sup>, L. Sanavia <sup>a</sup>, C. di Prisco <sup>b</sup> and F. Pisanò <sup>c</sup>**

4 <sup>a</sup>Department of Civil, Environmental and Architectural Engineering, University of Padova, Padova, Italy

5 <sup>b</sup>Department of Civil and Environmental Engineering, Politecnico di Milano, Milan, Italy

6 <sup>c</sup>Faculty of Civil Engineering and Geosciences, Delft University of Technology, Delft, Netherlands

7  
8 \* Corresponding author.

9 E-mail address: lazari.marial@gmail.com  
10

11 **ABSTRACT**

12 This paper reappraises Perzyna-type viscoplasticity for the constitutive modelling of granular  
13 geomaterials, with emphasis on the simulation of rate/time effects of different magnitude. An existing  
14 elasto-plastic model for sands is first recast into a Perzyna viscoplastic formulation, then  
15 calibrated/validated against laboratory test results on Hostun sand from the literature. Notable model  
16 features include (i) enhanced definition of the viscous nucleus function, and (ii) void ratio dependence  
17 of stiffness and viscous parameters, to model the pycnotropic behaviour of granular materials with a  
18 single set of parameters, uniquely identified against standard creep and triaxial test results. The  
19 comparison between experimental data and numerical simulations points out the predicative capability  
20 of the developed model and the complexity of defining a unique viscous nucleus function to capture  
21 sand behaviour under different loading/initial/boundary and drainage conditions. It is concluded that the  
22 unified viscoplastic simulation of both drained and undrained response is particularly challenging within  
23 Perzyna's framework and opens to future research in the area. The discussion presented is relevant, for  
24 instance, to the simulation of multi-phase strain localisation phenomena, such as those associated to  
25 slope stability problems in variably saturated soils.

26  
27 **Keywords:** sand, creep, constitutive modelling, Perzyna viscoplasticity, strain localisation,  
28 regularisation

29 **1 INTRODUCTION**

30 There is wide experimental evidence of granular geomaterials responding to external perturbations  
31 rapidly but not instantaneously. The microstructural rearrangements that cause macroscopic  
32 deformations take place over time frames sometimes in the order of minutes – such as in the case of  
33 loose sands [1]. Laboratory investigations regarding strain rate effects, creep and relaxation in sand have  
34 been presented in [1]–[8]. In light of those experimental observations, the mathematical modelling of

35 granular soil behaviour may be successfully tackled in the framework of delayed plasticity theories –  
36 also referred to as viscoplasticity – or through a viscous evanescent relationship. Most viscoplastic  
37 models are formulated according to either of two different approaches: those allowing the stress state to  
38 lie outside the assumed elastic domain [9], [10] and those relying on rate-dependent hardening rules  
39 (consistency viscoplasticity, [11]–[14]). Alternatively, [15]–[16] proposed a viscous evanescent  
40 relationship within a general three-component model framework. Here, the former approach in the  
41 version proposed by Perzyna [9], [17] will be followed due to its proven capability to reproduce the rate-  
42 dependence of both fine- and coarse-grained soils [18]–[21], including creep and relaxation phenomena.  
43 Importantly, Perzyna’s viscoplasticity has also proven a suitable conceptual platform for the  
44 interpretation of several soil instabilities ([19], [22]–[25]).

45 Viscoplasticity has also gained further success over the years as a regularisation technique for strain  
46 localisation simulations. This notable property relates to the intrinsic characteristic length possessed by  
47 viscoplastic media as a consequence of their time-sensitiveness ([11], [22], [26]–[30]). As a  
48 consequence, the ill-posedness of inviscid elasto-plastic problems at the onset of bifurcation can be  
49 remedied [31], as well as the pathologic mesh-dependence of corresponding finite element simulation  
50 results. Enhanced regularisation performance has also been achieved via a non-local reformulation of  
51 standard viscoplastic constitutive equations (e.g. [32], [33]). Such approach is beneficial for materials  
52 whose viscosity-related characteristic length is physically inaccurate, or in fact too small to produce any  
53 regularisation.

54 This work addresses the less investigated problem of formulating/calibrating viscoplastic models that  
55 can quantitatively capture the rate-dependent behaviour of sands under diverse loading/initial/boundary  
56 conditions. For this purpose, the existing elasto-plastic sand model by Buscarnera and Nova [34] (based  
57 on the previous work of Jommi [35], Jommi and di Prisco [36] and Nova et al. [37]) is reformulated  
58 according to Perzyna’s viscoplastic approach and validated against experimental data from the literature.  
59 Special attention is devoted to the importance of the viscous nucleus definition – main factor affecting  
60 the rate-sensitiveness – and to the intrinsic pycnotropy of sand behaviour (dependence on the void ratio).  
61 The latter aspect is addressed by introducing a straightforward void-ratio dependence of certain soil  
62 parameters (viscosity, stiffness and hardening coefficients), as already explored e.g. by [38].

63 The ultimate goal of the work is to re-open a discussion on the fundamental requisites of viscoplastic  
64 sand models, not solely in terms of their regularisation performance, but primarily of their physical  
65 soundness predictive capability.

## 2 CONSTITUTIVE FORMULATION

66

67 The proposed elasto-viscoplastic model is formulated hereafter under the assumption of isotropic  
 68 hydro-mechanical behaviour, also including the effects of variation in suction and/or degree of saturation  
 69 for generality. The model builds upon the isotropic hardening formulation for unsaturated soils proposed  
 70 in [34], based on the previous work of [35]–[37]. Direct notation is adopted, with boldface and lightface  
 71 italic symbols denoting tensors/vectors and scalars, respectively.

### 72 2.1 Stress/strain variables and elastic law

73 The small-strain multiaxial formulation of the model is based on the following definition of the  
 74 generalised effective Cauchy stress tensor  $\boldsymbol{\sigma}'$  [39], applicable to three-phase porous materials with  
 75 incompressible solid grains:

$$\boldsymbol{\sigma}' = \boldsymbol{\sigma} - S_w p^w \mathbf{1} - (1 - S_w) p^g \mathbf{1} \quad (1)$$

76 where  $\boldsymbol{\sigma}$  is the total Cauchy stress tensor,  $p^w$  and  $p^g$  the pressures of pore liquid water and gas,  $S_w$  the  
 77 water degree of saturation, and  $\mathbf{1}$  the second-order identity tensor. The cases of dry and water saturated  
 78 soil are recovered by setting  $S_w = 0$  and  $S_w = 1$ , respectively.

79 The total strain rate is decomposed additively into elastic/reversible ( $\dot{\boldsymbol{\epsilon}}^e$ ) and viscoplastic/irreversible ( $\dot{\boldsymbol{\epsilon}}^{vp}$ ) components:  
 80

$$\dot{\boldsymbol{\epsilon}} = \dot{\boldsymbol{\epsilon}}^e + \dot{\boldsymbol{\epsilon}}^{vp} \quad (2)$$

81 with the latter being by definition time-delayed. The elastic behaviour of the material emerges directly  
 82 from a strain energy function  $\psi(\boldsymbol{\epsilon}^e)$ :

$$\boldsymbol{\sigma}' = \frac{\partial \psi}{\partial \boldsymbol{\epsilon}^e}(\boldsymbol{\epsilon}^e) \quad (3)$$

83 and can be then cast into the following rate form:

$$\dot{\boldsymbol{\sigma}}' = \mathbf{D}^e [\dot{\boldsymbol{\epsilon}} - \dot{\boldsymbol{\epsilon}}^{vp}] \quad (4)$$

84 In Equation (4)  $\mathbf{D}^e$  is the fourth-order elastic stiffness tensor given by:

$$\mathbf{D}^e = \frac{\partial^2 \psi(\boldsymbol{\epsilon}^e)}{\partial \boldsymbol{\epsilon}^e \otimes \partial \boldsymbol{\epsilon}^e} \quad (5)$$

85 with  $\psi(\boldsymbol{\epsilon}^e)$  being the same stored energy function already adopted by [37], [40], [41] – see Appendix  
 86 for more details.

87 2.2 Yield function and plastic potential

88 Yield and plastic potential functions are defined as proposed in [42]:

$$\left. \begin{matrix} f \\ g \end{matrix} \right\} = A_h^{K_{-z}/C_h} B_h^{-K_{2h}/C_h} p' - p'_{sh} = 0 \quad (6)$$

89 with

$$\left. \begin{matrix} K_{1h} \\ K_{2h} \end{matrix} \right\} = \frac{m_h(1-\alpha_h)}{2(1-m_h)} \left\{ 1 \pm \sqrt{1 - \frac{4\alpha_h(1-m_h)}{m_h(1-\alpha_h)^2}} \right\} \quad (7)$$

90

$$\begin{aligned} A_h &= 1 + \frac{1}{K_{1h} M_h(S)} \frac{q}{p'} \\ B_h &= 1 + \frac{1}{K_{2h} M_h(S)} \frac{q}{p'} \\ C_h &= (1-m_h)(K_{1h} - K_{2h}) \end{aligned} \quad (8)$$

91 where the subscript  $h = f, g$  is used to indicate either the yield function or the plastic potential. In

92 Equations (6)–(8)  $m_h$  and  $\alpha_h$  are constitutive parameters (see Table 1). The interested reader is referred

93 to [34], [41], [42], where the physical meaning of relevant model parameters is described.

94 The current stress state is represented through the following three invariants:

$$p' = \frac{1}{3} \text{tr}(\boldsymbol{\sigma}') \quad q = \sqrt{\frac{3}{2}} \|\mathbf{s}\| \quad S = \sin(3\theta) = \sqrt{6} \frac{\text{tr}(\mathbf{s}^3)}{[\text{tr}(\mathbf{s}^2)]^{3/2}} \quad (9)$$

95 where  $p'$  is the mean effective stress,  $q$  the deviator stress (proportional to the norm of the deviator stress

96 tensor  $\mathbf{s}$ ), and  $S$  a trigonometric function of the Lode angle  $\theta$  (with  $\theta$  equal to  $30^\circ$  in triaxial compression

97 and  $-30^\circ$  in triaxial extension). The variable  $M_h(S)$  in Equation (8) is given after [43]:

$$M_h(S) = \frac{2cM_{ch}}{(1+c) - (1-c)S} \quad c = \frac{M_{eh}}{M_{ch}} \quad (10)$$

98 in which  $M_c$  and  $M_e$  are the values of  $M(S)$  associated with triaxial compression and extension,

99 respectively. The internal variables  $p'_{sh}$  in Equation (6) govern the size of the yield locus and plastic

100 potential in the effective stress space. In the following,  $p'_{sf}$  is simply denoted as  $p'_s$  and termed pre-

101 consolidation stress, while  $p'_{sg}$  is a dummy variable that does not affect the stress gradient of  $g$ .

102 2.3 *Viscoplastic flow rule*

103 The rate of viscoplastic strains is obtained according to the well-known approach proposed by Perzyna  
 104 [9], [17]:

$$\dot{\boldsymbol{\varepsilon}}^{\text{vp}} = \gamma \Phi(f) \frac{\partial g}{\partial \boldsymbol{\sigma}'} \quad (11)$$

105 where  $f$  and  $g$  keep denoting yield and plastic potential functions (Equation (6)), and  $\Phi$  is commonly  
 106 referred to as “viscous nucleus”. In the same equation, the so-called “fluidity parameter”  $\gamma$  governs the  
 107 rate-sensitiveness of the solid skeleton ( $\gamma=1/\eta$ , with  $\eta$  viscosity) and specifically the rate at which  
 108 viscoplastic strains occur. Increasing  $\gamma$  values reduce the rate-sensitiveness of the material: when  $\gamma \rightarrow \infty$   
 109 the mechanical response tends to its elasto-plastic (rate-insensitive) limit. At variance with rate-  
 110 independent plasticity, the magnitude of the viscoplastic strain rate results directly from the scalar  
 111 “distance”  $\Phi$  between the current stress point and the yield locus (overstress), with no enforcement of  
 112 the usual consistency condition. The direction of the instantaneous viscoplastic flow is still governed by  
 113 the gradient of the plastic potential  $g$ .

114 The selection of the viscous nucleus function is a distinctive feature of elasto-viscoplastic Perzyna  
 115 models. It must be formulated and calibrated to pursue best agreement with experimental data from  
 116 standard creep tests, particularly by mobilising in experiments different levels of overstress. It should be  
 117 noted that the shape of the viscous nucleus function (and associated parameters) is model-specific, i.e.  
 118 affected by all other (elasto-plastic) features of the model. A more comprehensive discussion on this  
 119 matter can be found in [1]. Herein, the implications of two different definitions are discussed:

- 120 • power-law viscous nucleus, most common in the literature [11]:

$$\Phi(f) = \left\langle \left( \frac{f}{|p'|} \right)^\alpha \right\rangle = \langle \bar{f}^\alpha \rangle \quad (12)$$

- 121 • exponential viscous nucleus, initially proposed in [1] for loose sands:

$$\Phi(f) = e^{\alpha \bar{f}} \quad (13)$$

122 where  $\alpha$  is in the above definitions an additional viscous parameter controlling the shape of the viscous  
 123 nucleus function (Table 1). The Macaulay brackets  $\langle \rangle$  are used in Equation (12) according their usual  
 124 meaning:

$$\langle \bar{f}^\alpha \rangle = \begin{cases} \bar{f}^\alpha & \text{if } \bar{f}^\alpha \geq 0 \\ 0 & \text{if } \bar{f}^\alpha < 0 \end{cases} \quad (14)$$

125 to make irreversible viscoplastic strains only occur when the stress state lies outside the elastic domain  
 126 (i.e. when  $f > 0$ ). Both expressions (12) - (13) fulfil the relevant theoretical requirements discussed by  
 127 [1], while the use of the dimensionless yield function  $\bar{f}$  is appropriate for pressure-sensitive materials  
 128 [44], [45].

#### 129 2.4 Hardening rule

130 Under general hydro-mechanical loading paths, the preconsolidation stress  $p'_s$  evolves according to  
 131 the following hardening rule [34], [35]:

$$\dot{p}'_s = \rho_s p'_s (\dot{\varepsilon}_v^{vp} + \zeta_s \dot{\varepsilon}_s^{vp}) - r_{sw} p'_s \dot{S}_w \quad (15)$$

132 where  $\rho_s$ ,  $\zeta_s$  and  $r_{sw}$  are material parameters governing mechanical and hydraulic hardening, respectively  
 133 (Table 1). In particular, the second term at the right-hand side of Equation (15) models  
 134 phenomenologically the hydraulic bonding effect characterising the response of unsaturated soils. In  
 135 Equation (15),  $\dot{\varepsilon}_v^{vp}$  and  $\dot{\varepsilon}_s^{vp}$  are the rates of volumetric and deviatoric viscoplastic strains respectively:

$$\varepsilon_v = \boldsymbol{\varepsilon} : \mathbf{1} \quad ; \quad \varepsilon_s = \sqrt{\frac{2}{3}} \|\mathbf{e}\| \quad ; \quad \dot{\varepsilon}_v = \dot{\boldsymbol{\varepsilon}} : \mathbf{1} \quad ; \quad \dot{\varepsilon}_s = \sqrt{\frac{2}{3}} \|\dot{\mathbf{e}}\| \quad (16)$$

136 where  $\boldsymbol{\varepsilon}$  is the strain tensor,  $\varepsilon_v$  the volumetric strain,  $\varepsilon_s$  the deviatoric strain and  $\mathbf{e}$  is the deviatoric  
 137 component of the strain tensor:

$$\mathbf{e} = \boldsymbol{\varepsilon} - \frac{1}{3} \text{tr}(\boldsymbol{\varepsilon}) \mathbf{1} \quad ; \quad \dot{\mathbf{e}} = \dot{\boldsymbol{\varepsilon}} - \frac{1}{3} \text{tr}(\dot{\boldsymbol{\varepsilon}}) \mathbf{1} \quad (17)$$

#### 138 2.5 Influence of relative density

139 Granular materials respond to mechanical perturbations depending on the current void ratio  
 140 (pycnotropy) and effective confining pressure (barotropy). This essential feature has been successfully  
 141 captured in the literature through the notion of “state parameter”, which enables to reproduce the  
 142 behaviour of loose-to-dense materials with a single set of parameters [46]–[51].

143 Herein, the simpler approach proposed in [38] has been preferred to exploit the lack of the so-called  
 144 consistency condition. Accordingly, it is possible to incorporate pycnotropy into the viscoplastic  
 145 formulation by modulating certain constitutive parameters according to the current relative density (or  
 146 void ratio). This allows to describe the main consequences of dense-to-loose transitions (and vice versa),  
 147 such as softening and vanishing dilatancy at medium/large strains [32], [38]. As originally proposed in  
 148 [38], a linear dependence on the relative density is assumed here for the viscosity  $\eta$ , the representative  
 149 elastic shear modulus ( $G_0$ ) and the hardening parameter  $r_{sw}$ :

$$p_i = p_{Li} + (p_{Di} - p_{Li}) \cdot D_r \quad (18)$$

150 in which the value of the generic parameter  $p_i$  depends on the current relative density  $D_r$  and two  
 151 bounding values,  $p_{Li}$  and  $p_{Di}$ , set for the loosest and densest reference conditions – here  $D_r = 20\%$  and  
 152  $D_r = 100\%$  respectively. Current  $D_r$  value is updated at each integration step based on the evolving soil  
 153 volumetric strain [38]. However, such a linear dependence should not be taken for granted, and indeed  
 154 the following non-linear relationship has been found to perform better for the constitutive parameters  $\zeta_s$   
 155 and  $\rho_s$  (see Section 4.1 and [52]):

$$p_i = p_{Li} + (p_{Di} - p_{Li}) D_r^{5(e_{max} - e_{min})} \quad (19)$$

156 where in this case  $p_i$  represents either  $\zeta_s$  or  $\rho_s$ , while  $e_{max}/e_{min}$  are the maximum/minimum void ratios of  
 157 the sand. In the spirit of the present viscoplastic approach, pycnotropy can be simply reproduced through  
 158 density-dependent parameters. Nonetheless, specific  $D_r$ -dependences need to be identified by  
 159 comparison to experimental results, and may assume the forms exemplified by Equations (18)-(19).

160 A synopsis of all constitutive parameters and their meaning is given in Table 1. The model as  
 161 formulated above is suited for hydro-mechanical processes involving unsaturated conditions and viscous  
 162 effects. Its performance in presence of strain localisation problems may be fully regularised by coupling  
 163 viscoplasticity and extension to non-locality ([53]–[55]). This can be easily achieved through a non-  
 164 local reformulation of the viscoplastic flow-rule Equation (11), as successfully attempted in a few  
 165 previous works of the authors ([32], [33], [44], [38], [56]–[58]).

166 The following sections address the calibration and validation of the proposed constitutive model  
 167 against the response of clean Hostun sand. Although conceived for generally unsaturated sands, the  
 168 model will be solely tested for either saturated or dry conditions, due to the dearth of test data regarding  
 169 the rate-sensitiveness of unsaturated sands. The goal is to investigate to what extent a single set of elastic,  
 170 plastic and viscous parameters can be identified to capture sand response over a wide range of relative  
 171 density, initial/drainage conditions, loading rate and stress paths.

172 The model described above has been implemented in the finite element code for multiphase porous  
 173 media Comes-Geo, developed at the University of Padova ([33], [59]–[66]). All the numerical results  
 174 have been obtained via explicit forward Euler stress-point integration [67], [68] after preliminary  
 175 verification of the numerical implementation (see [52]) against the simulation results in Buscarnera and  
 176 Nova (2009)<sup>1</sup>.

<sup>1</sup> It is always possible to compare the performance of a viscoplastic model to the response of its elasto-plastic (rate-insensitive) counterpart by simply setting a sufficiently high fluidity parameter  $\gamma$  in Equation (11).

177

### 3 MODEL CALIBRATION FOR LOOSE AND DENSE HOSTUN SAND

178

All constitutive parameters have been calibrated based on literature triaxial and creep tests on Hostun

179

sand, allowing a separate identification of elasto-plastic and viscous parameters, respectively. Table 2

180

summarises the main features (drainage, initial confinement and void ratio) of the reference tests from

181

[50], [1], [8], [69]-[70] – the same test labels as in the original publications have been kept in the

182

following.

183

#### 3.1 Elasto-plastic parameters

184

The parameters governing the elasto-plastic behaviour have been calibrated by assuming a very high

185

loading rate, i.e. by artificially forcing the response of the viscoplastic model towards its rate-insensitive

186

limit. For this purpose the triaxial test results labelled in Table 2 as *hos027 d4*, *batr02* and *alert9* have

187

been best-matched as exemplified in Figure 1. The final set of calibrated elasto-plastic parameters is

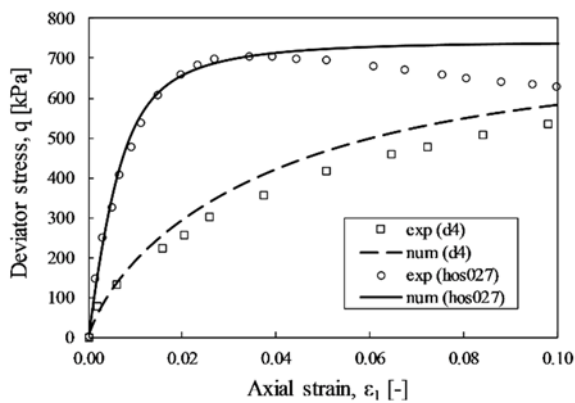
188

reported in Table 3 and Table 4, with the latter providing the loose-to-dense range of  $D_r$ -dependent

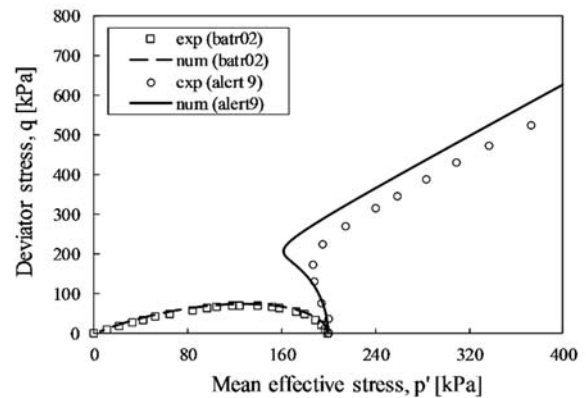
189

parameters.

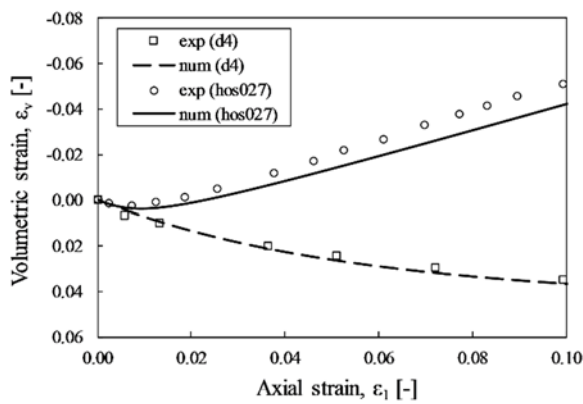
190



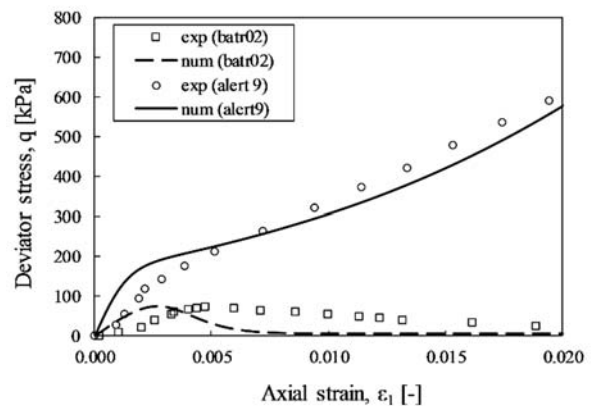
(a)



(b)



(c)



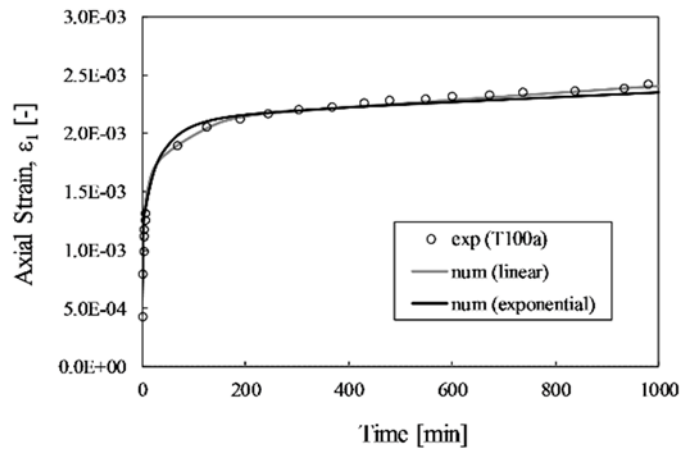
(d)

Figure 1: Calibration of elasto-plastic parameters against (a), (c) drained and (b), (d) undrained triaxial test results for loose (*d4, batr02*) and dense (*hos027, alert9*) Hostun sand.

191 3.2 Viscous parameters

192 With the same set of elasto-plastic parameters (Tables 3-4), the viscous parameters of Hostun loose  
 193 and dense sand have been separately identified through the drained creep test results from [1] and [8].  
 194 di Prisco and Imposimato [1] performed tests on loose Hostun sand ( $D_r = 20\%$ ) by holding the radial  
 195 effective stress constant while increasing the axial component up to attain the target stress obliquity;  
 196 subsequent axial stress increments have been then applied with a five minutes time lag to explore the  
 197 creep response. Two sets of viscous parameters have been calibrated for the different viscous nucleus  
 198 definitions in Equations (12)-(13), namely linear ( $\alpha=1$  in the power-law expression) and exponential.  
 199 With reference to the last creep step in the original publication (approximately 15 minutes duration),  
 200 Figure 2 shows the axial strain vs time performance of the model (solid lines) in comparison to the  
 201 experimental data from [1] (circular markers). It is readily apparent that satisfactory agreement can be  
 202 achieved in this case regardless of the adopted viscous nucleus, as long as suitable (and nucleus-specific)  
 203 viscous parameters are set (see Table 5).

204



205

206 Figure 2: Simulation of loose Hostun sand creep by using linear and exponential viscous nuclei  
 207 ( $e_{\sigma}=0.950, p'_{\sigma}=100$  kPa): axial strain vs time.  
 208

209 The viscous parameters for Hostun dense sand ( $D_r = 71\%$ ) have been then derived based on the  
 210 experimental results from [8] and reported in Table 6. It should be noted that the same value of  $\alpha$  (i.e.  
 211 same shape of  $\Phi$ ) has been used for both loose and dense Hostun sand (see Table 5 and Table 6) to  
 212 reduce the number of free parameters. Such assumption is reasonably confirmed by data/simulations  
 213 presented herein for Hostun sand, although future confirmation for different materials is needed. The

<sup>2</sup> Given the low viscosity of dense sands, the viscosity identified for  $D_r = 71\%$  has been used as  $p_D$  in Eq. (18).

214 laboratory experiments were performed by initially consolidating the sample under an effective mean  
 215 pressure of 80 kPa, then followed by drained triaxial compression; the triaxial compression load path  
 216 included three additional stages of creep and cyclic loading, as illustrated in Figure 3.

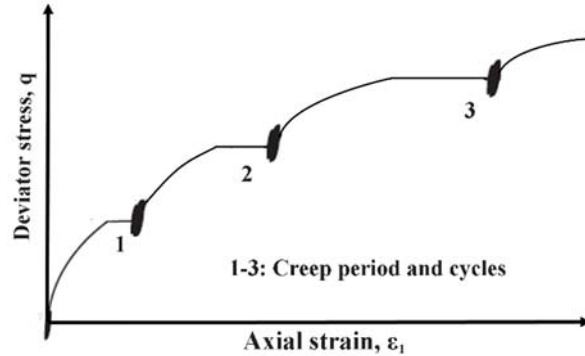


Figure 3: Creep test on dense Hostun sand (after [8]).

217  
 218 Experimental and numerical stress-strain curves are presented in Figure 4a for all four creep stages – no  
 219 intermediate cyclic loading simulated. For clearer visualisation in Figure 4b, the numerical axial strains  
 220 developed during creep after each triaxial compression are compared to the experimental results only  
 221 for the case of exponential viscous nucleus.

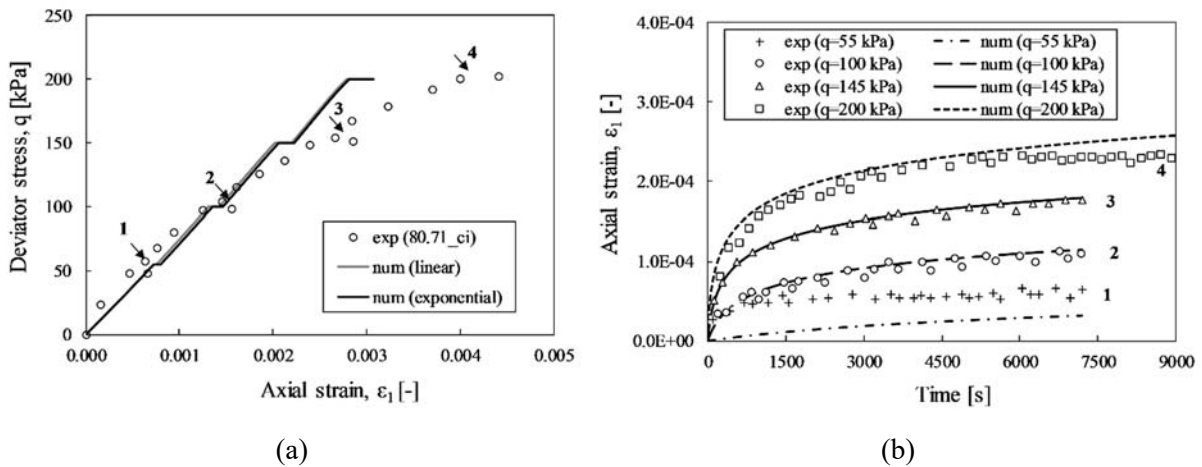


Figure 4: Simulation of creep behaviour for dense Hostun sand ( $e_0=0.710$ ,  $p'_0=80$  kPa): (a) global stress-strain response and (b) time evolution of axial strain.

222 The viscoplastic model reproduces with sufficient accuracy the response to all creep stages, though  
 223 with some visible deviations from the global stress-strain behaviour (possibly affected by neglecting  
 224 intermediate cyclic loading in the numerical simulations). Comparing the creep responses of loose and  
 225 dense Hostun sands points out more significant time effects for the former – in expected agreement with  
 226 the experimental literature.

## 4 MODEL VALIDATION

227

228 After the above parameter calibration, the full elasto-viscoplastic model is validated against the data set  
229 overviewed in Table 2. Such a validation is carried out for Hostun sand at two levels: (i) against triaxial  
230 test results already used for the calibration of elasto-plastic parameters (Section 3.1); (ii) against different  
231 experimental results – not previously considered – to produce valuable blind predictions. It should be  
232 noted that the validation level (i) is still necessary to check whether the parameters derived from creep  
233 tests produce appropriate time-sensitiveness when combined with different loading rate and test  
234 conditions. The suitability of assuming  $D_r$ -dependent constitutive parameters is also highlighted in this  
235 section.

236 All numerical simulations have been performed at imposed displacement rates of 1 mm/min and 2  
237 mm/min for drained and undrained triaxial tests, respectively [72] – unless differently specified.

### 238 4.1 Drained triaxial compression tests (TXD)

239 The model is first validated against the experimental results of TXD tests at varying relative density  
240 and effective confinement. The predicted responses arising from the above viscous nucleus definitions  
241 are also critically compared, with all relevant material parameters listed in Table 3 to Table 6. A linear  
242  $D_r$ -dependence (Equation (18)) is in some instances applied to all variable parameters, so as to point out  
243 the better performance the non-linear relationship (19) conclusively applied to the parameters  $\xi_s$  and  $\rho_s$ .  
244 Further insight into the accuracy of the model is provided by comparison to the elasto-plastic predictions  
245 obtained through the kinematic-hardening constitutive model of Gajo and Wood [50].

#### 246 4.1.1 Loose Hostun sand

247 The outcomes of the two different viscous nuclei (Equations (12)-(13)) are compared in Figure 5 for  
248 the TXD response of a loose sample ( $d4$  in Table 2). The results clearly witness the superior performance  
249 of the non-linear/exponential viscous nucleus, which confirms the quite complex dependence of sand  
250 viscosity on the overstress level (i.e. on the value of  $f$ ). It should be noted that the mismatching TXD  
251 predictions in Figure 5 come after the same level of accuracy achieved by both viscous nuclei in slow  
252 creep tests (Figure 2). This conclusion is also confirmed by the cases of medium dense and dense Hostun  
253 sand discussed in the following.

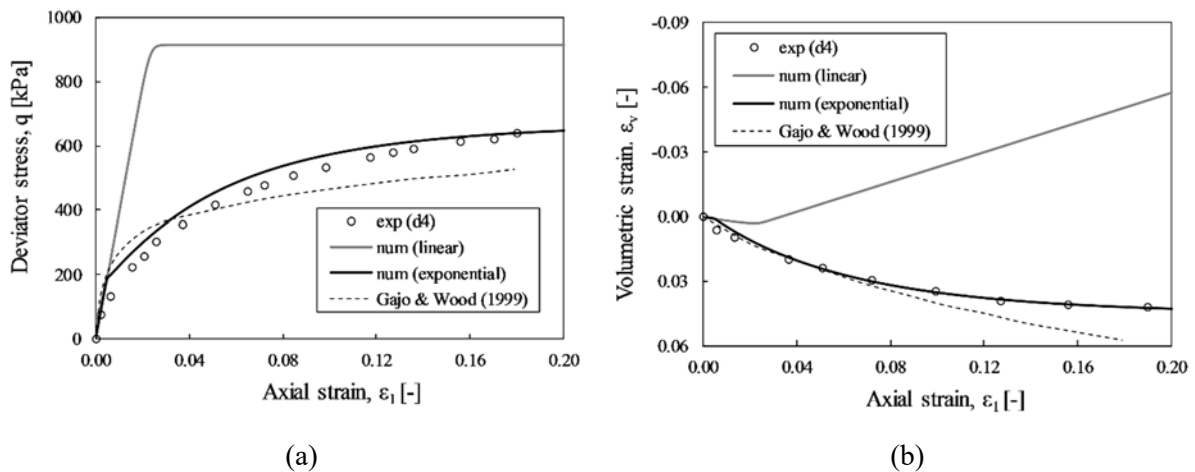


Figure 5: TXD test on loose Hostun sand ( $e_0=0.945$ ,  $p'_o=300$  kPa): (a) deviatoric stress-strain response and (b) volumetric behaviour.

254

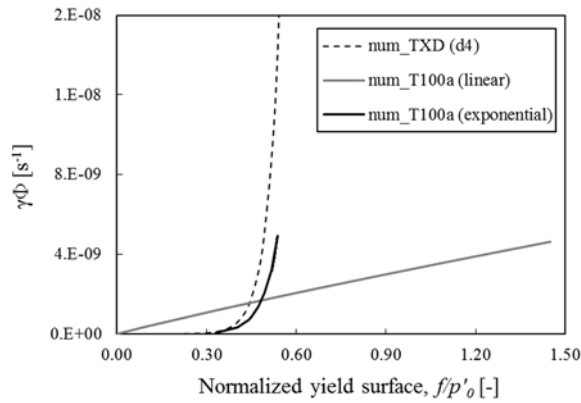


Figure 6: Evolution of the  $\gamma\Phi$  product for creep (*T100a*) and TXD (*d4*) tests on loose Hostun sand.

255 The applicability of the exponential viscous nucleus is underpinned by Figure 6, where the evolution of  
 256 the  $\gamma\Phi$  product (fluidity parameter times viscous nucleus) is plotted against the yield function values for  
 257 the above TXD (*d4*) and creep (*T100a*) tests. Apparently, the linear viscous nucleus leads to very high  
 258 values of the yield surface, at variance with the exponential formulation. This stems from the interaction  
 259 between the functions assumed in this study for the viscous nucleus and the yield locus [42], with the  
 260 latter being in turn a (very) non-linear function of the (over)stress state. The effect of such interaction  
 261 stands out under high(er) overstress levels, therefore more clearly under traxial loading than during  
 262 creep.

#### 263 4.1.2 Dense Hostun sand

264 The comparison between experimental and numerical dense sand behaviour is illustrated in Figure 7  
 265 (*hos027* in Table 2). As in the loose sand case, the results from the linear viscous nucleus are quite  
 266 unsatisfactory: the peak stress is significantly underestimated (Figure 7a), while the predicted volumetric

267 strain trend is less dilatative than in reality (Figure 7b). Conversely, the use of exponential nucleus allows  
 268 to capture correctly both the peak stress and the dilatancy, although the strain softening behaviour can  
 269 only be reproduced via the non-linear  $D_r$ -dependence of  $\zeta_s$  and  $\rho_s$  (Equation (19)).

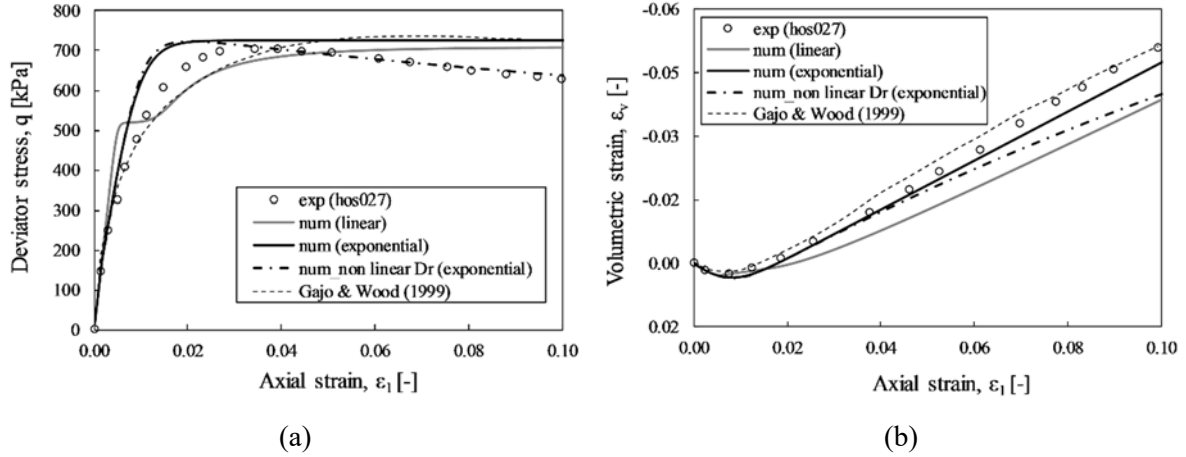


Figure 7: TXD test on dense Hostun sand ( $e_0=0.578$ ,  $p'_0=200$  kPa): (a) deviatoric stress-strain response and (b) volumetric behaviour.

#### 270 4.1.3 Medium dense Hostun sand

271 The TXD tests on medium-dense Hostun sand are well simulated by the model enhanced with non-  
 272 linear  $D_r$ -dependence – see Figure 8. The peak deviator stress is perfectly matched in Figure 8a, as well  
 273 as the overall volumetric response in Figure 8b.

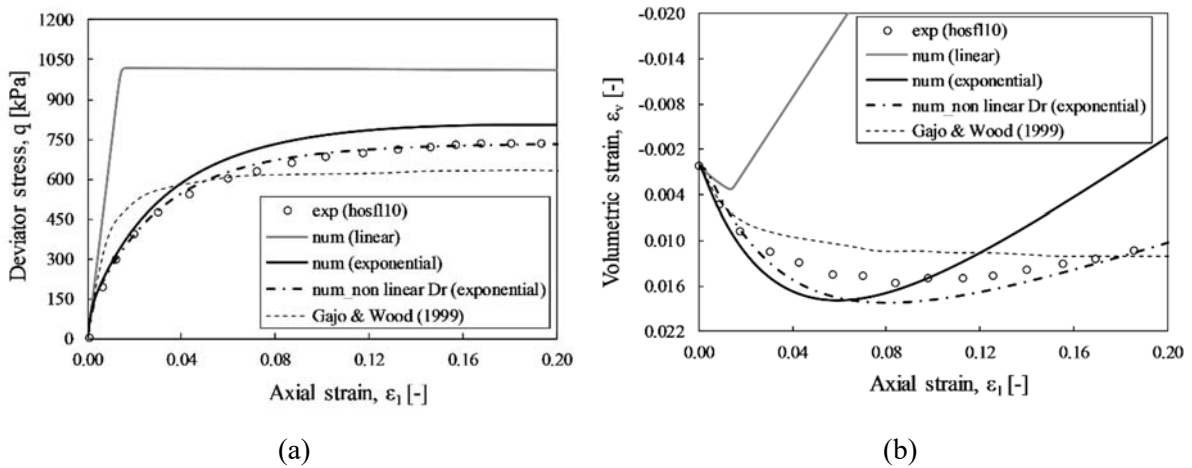


Figure 8: TXD test on medium-dense Hostun sand ( $e_0=0.8$ ,  $p'_0=300$  kPa): (a) deviatoric stress-strain response and (b) volumetric behaviour.

#### 274 4.1.4 Further TXD model predictions

275 Additional TXD predictions are reported hereafter to further validate the viscoplastic model in its final  
 276 version with exponential viscous nucleus and non-linear  $D_r$ -dependence of the hardening parameters in  
 277 Equation (19). Experimental vs numerical comparisons are given in Figure 9 for TXD tests on loose

278 Hostun samples at different confining pressures, namely 100 (CD-1), 300 (CD-2) and 750 (CD-3) kPa  
 279 – experimental data from [69].

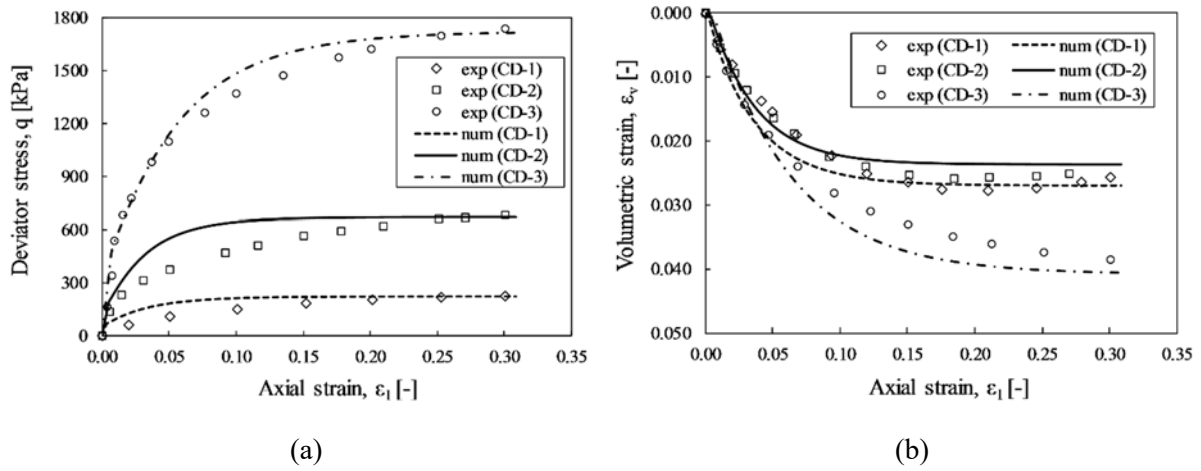


Figure 9: TXD tests on loose Hostun sand at varying effective confinement ( $e_0=0.954-1.052$ ,  $p'_0=100, 300, 750$  kPa): (a) deviatoric stress-stress response and (b) volumetric behaviour.

280 The stress-strain curves and volumetric trends in Figure 9 confirm that model can capture the intrinsic  
 281 pressure-dependence of sand behaviour at a given relative density ( $Dr \approx 10\%$ ), with rate-effects  
 282 spontaneously accommodated by the combination of suitable viscous parameters and realistic TXD  
 283 loading rate. Relatedly, Figure 10 presents the model predictions obtained for dense and loose Hostun  
 284 samples initially consolidated under the same isotropic pressure of 300 kPa. For the dense sample, both  
 285 strain softening behaviour (Figure 10a) and dilation (Figure 10b) are satisfactorily simulated with respect  
 286 to the experimental results from [50] – test *hos011* in Table 2. Similar conclusions may be extended to  
 287 the loose sample case – test *hosf111* (Figure 10c-d).

288 Figure 11, shows the case of two medium dense Hostun specimens initially consolidated at either low  
 289 or medium/high effective pressures, 50 kPa (test *hosf114*) and 600 kPa (test *hflw10*). As expected, the  
 290 performance of the model is slightly worse – though not dramatically – for intermediate void ratios, for  
 291 which more accurate modelling of barotropy/pycnotropy is likely needed.

292 The last TXD simulations in Figure 12 allow to further inspect the rate-sensitiveness of the monotonic  
 293 triaxial response. For this purpose, the experimental results on air-dried loose Hostun sand from [8] have  
 294 been considered, including isotropic consolidation up to 400 kPa followed by axial straining at two  
 295 different rates – one 10 times larger than the other. Even though Perzyna-type models are necessarily  
 296 sensitive to the loading rate until the inviscid limit, such sensitivity must be quantitatively compared to  
 297 experimental evidence. In agreement with previous/related sources (see e.g. [3], [15]), the experimental  
 298 results in Figure 12 confirm negligible rate-dependence of Hostun sand at the considered constant strain  
 299 rates – note the almost coincident stress-strain curves. Elasto-viscoplastic simulations with unaltered

300 constitutive parameters display in this case underpredicted sand stiffness, but confirm the observed low  
 301 rate-sensitiveness of the material. The merit for the latter outcome comes mostly from the adopted  
 302 viscous nucleus formulation, suitable to capture (drained) rate-sensitiveness over a wide overstress  
 303 range.

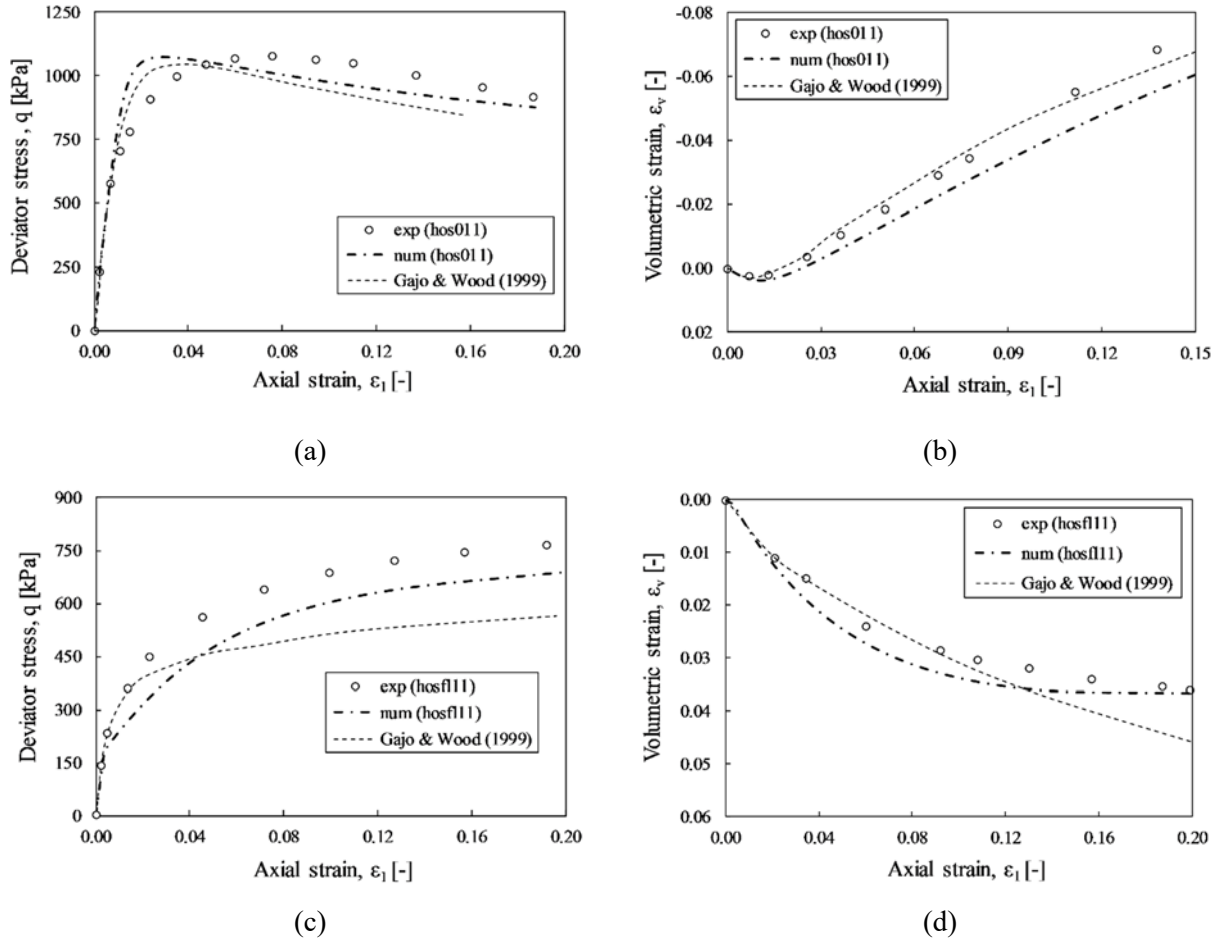


Figure 10: TXD tests on dense ( $e_0=0.574$ ) and loose ( $e_0=0.897$ ) Hostun sand at the same effective confinement ( $p'_0=300$  kPa): (a)-(c) deviatoric stress-stress response and (b)-(d) volumetric behaviour.

304  
 305 Overall, the results in this section show good ability of the model to reproduce TXD tests at varying  
 306 initial void ratio, effective confinement and loading rate, with viscous parameters independently  
 307 identified from creep experiments. This achievement is not dramatically affected by the unavoidable  
 308 heterogeneity of materials, facilities and operators in the reference experimental studies.

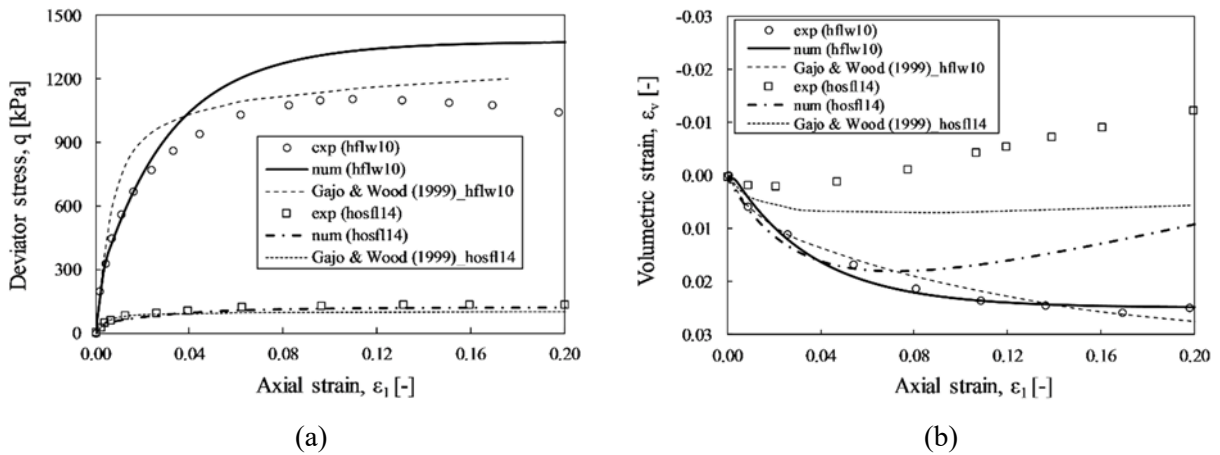


Figure 11: TXD tests on medium dense ( $e_0 = 0.822-0.838$ ) Hostun sand and different effective confinement ( $p'_0=50, 600$  kPa): (a) deviatoric stress-stress response and (b) volumetric behaviour.

309

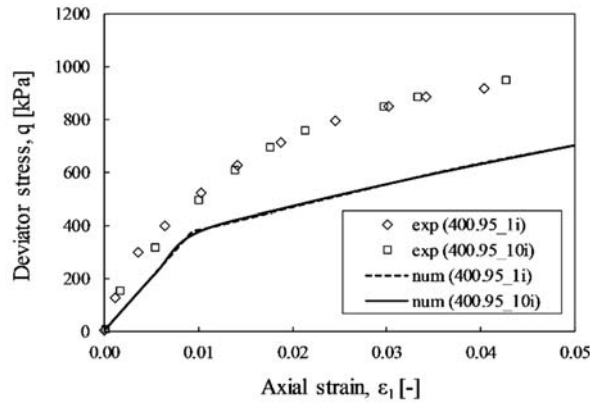


Figure 12: TXD on air-dried loose Hostun sand ( $e_0 = 0.95$ ) performed, respectively, at a strain rate of  $\dot{\epsilon}_0 = 0.06$  %/min, test 400.95 1i and  $\dot{\epsilon}_0 = 0.6$  %/min, test 400.95 10i (data from [8]<sup>3</sup>).

310 4.2 Undrained triaxial compression tests (TXU)

311 In this subsection the undrained triaxial performance of the proposed model is explored with respect  
 312 to the TXU tests in Table 2. It is noted that transiting to undrained conditions jeopardises the suitability  
 313 of the viscous parameters in Tables 5-6, which leads to envisage  $\Phi(f)$  function probably more complex  
 314 than the assumed exponential form [56]. The different stress paths characterising TXD and TXU tests  
 315 mobilise different ranges of the  $\Phi$ - $f$  relationship, whose non-linearity should be captured for accurate  
 316 simulations over a wide spectrum of loading conditions. Relatedly, simplistic viscous nucleus

<sup>3</sup> Intermediate relaxation branches in the original data have been removed from the plot, as overlooked in the numerical simulations for the sake of simplicity.

317 formulation conceived, for instance, for numerical regularisation purposes, may yield misleading results  
 318 when applied to very diverse loading/drainage conditions.

319 The parameters of the exponential viscous nucleus have been thus recalibrated based on the TXU  
 320 results in Figures 13-14, for loose and dense Hostun sand respectively – tests *batr02* and *alert9* from  
 321 [50]. The same figures indicate that the new viscous parameters in Table 7 along with the above elasto-  
 322 plastic parameters (Tables 3-4) result in reasonable simulations of undrained stress paths and deviatoric  
 323 stress-stress responses for both loose and dense samples. It is also worth observing that the  $D_r$ -  
 324 dependence of constitutive parameters is here only relevant to setting proper initial conditions, as the  
 325 void ratio does not vary during TXU loading.

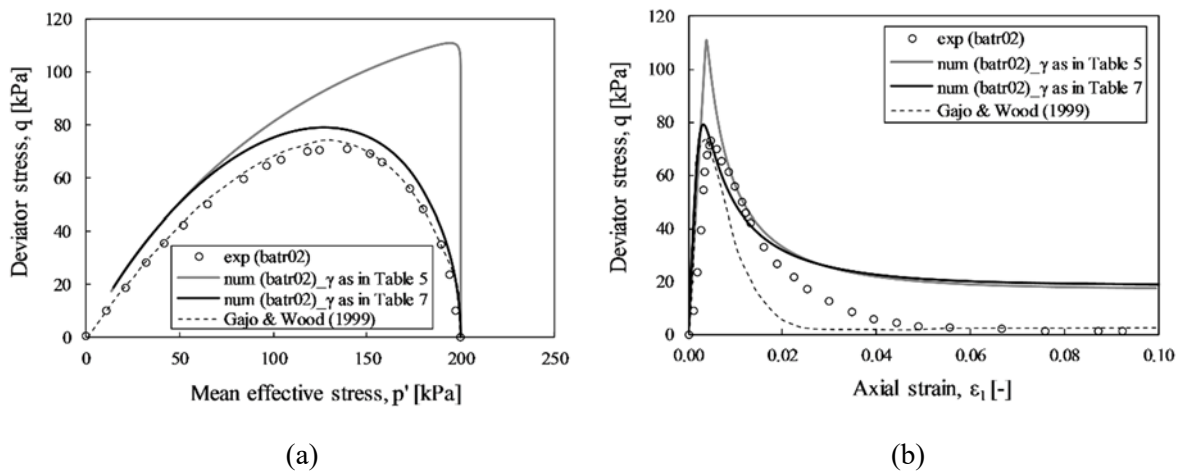


Figure 13: Re-calibration of the viscous parameters against TXU test on loose Hostun sand ( $e_0=0.940$ ,  $p'_0=200$  kPa): (a) stress path and (b) deviatoric stress-stain response.

326

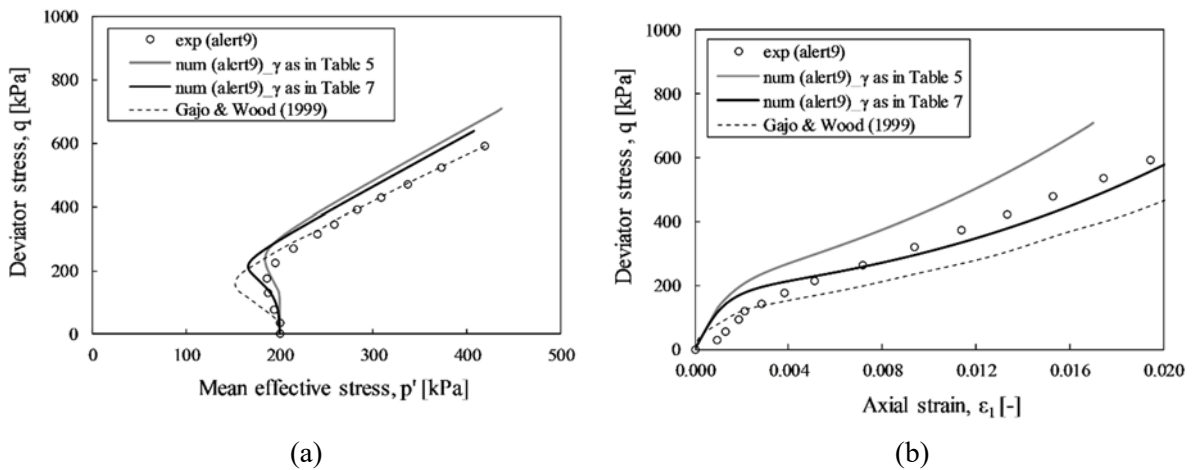


Figure 14: Re-calibration of the viscous parameters against TXU test on dense Hostun sand ( $e_0=0.666$ ,  $p'_0=200$  kPa): (a) stress path and (b) deviatoric stress-stain response.

327

328 After the identification of “undrained” viscous parameters, TXU tests on loose and medium-dense  
 329 Hostun specimens have been considered for re-validation. The results in Figure 15 concern the tests  
 330 from [69] on loose sand at initial confinement equal to 750kPa (*ICU-1*), 300kPa (*ICU-2*) and 100kPa  
 331 (*ICU-3*). Encouraging numerical predictions have been found again in all relevant respects, and  
 332 particularly in terms of undrained stress path and pore pressure build-up. Similar satisfactory results can  
 333 be seen in Figure 16 for the medium dense sand tested by [50] – test *batr06*.  
 334

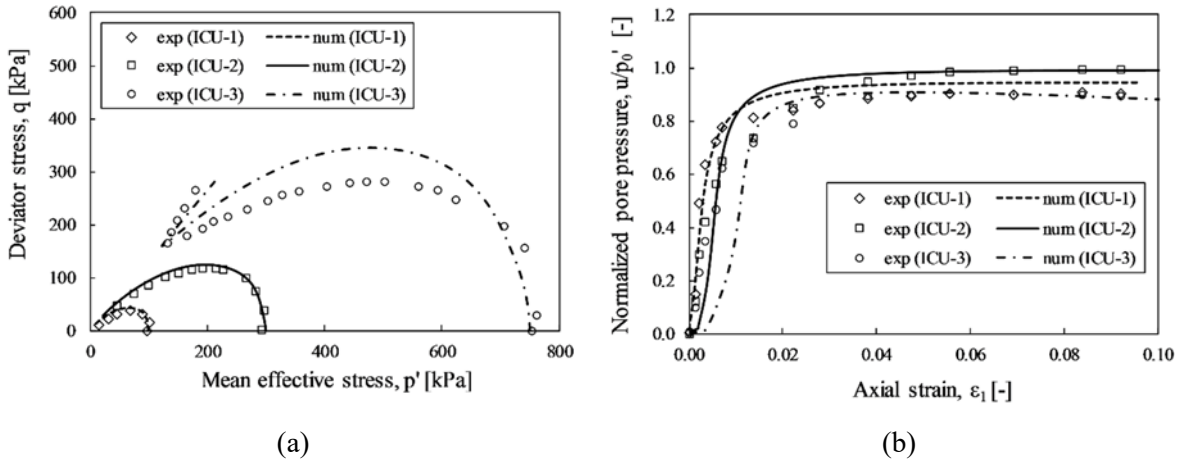


Figure 15: TXU tests on loose Hostun sand at varying effective confinement ( $e_0=1.060-1.083$ ,  $p'_0=100, 300, 750$  kPa): (a) stress path and (b) normalized pore pressure versus axial strain.

335

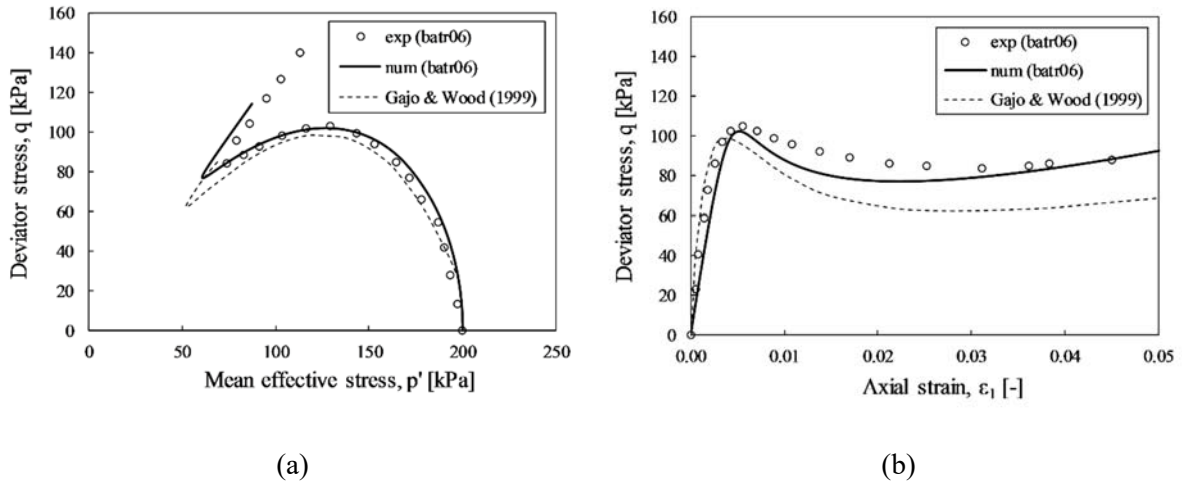


Figure 16: TXU on medium-dense ( $e_0=0.830$ ,  $p'_0=200$  kPa) Hostun sand: (a) stress path and (b) deviatoric stress-stain response.

336

337 4.3 *Undrained plane-strain/biaxial compression test*

338 Further validation has been successfully sought against the biaxial undrained test results documented  
339 in [70] – test *SHFND05*,  $p'_{\sigma}=800$  kPa, axial displacement rate equal to 1.2 mm/min. Similarly to drained  
340 conditions, the model endowed with its “undrained” viscous nucleus is capable to blindly predict other  
341 experimental data not used for calibration. Specifically, Figure 17 illustrates the excellent agreement  
342 achieved in terms of stress path, stress-strain response and pore pressure build up.

343 4.4 *Undrained creep tests*

344 The results of (rare) undrained creep tests on Hostun loose sand are used as a final benchmark – data  
345 from [71]. The original experimental tests were conducted with undrained creep following a preliminary  
346 TXD stage up to target stress obliquity. Such a loading programme (test *20DP13*) has been simulated  
347 with the same parameters mentioned in Sections 4.2-4.3. During the TXD phase small load increments  
348 were applied: between two subsequent load increments a time period of 5 minutes elapsed; when the  
349 desired stress level was reached ( $q = 61$  kPa,  $p' = 120$  kPa) a further load increment of 2 kPa was applied.  
350 The predictions in Figure 18 obtained for the creep stage show reasonable agreement in terms of axial  
351 strain and pore pressure. The premature onset of creep instability (inflection point in the pore pressure  
352 curve) is most likely due to the specific yield function shape and the (simplistic) assumption of isotropic  
353 hardening ([25], [75]), rather than to viscous modelling.

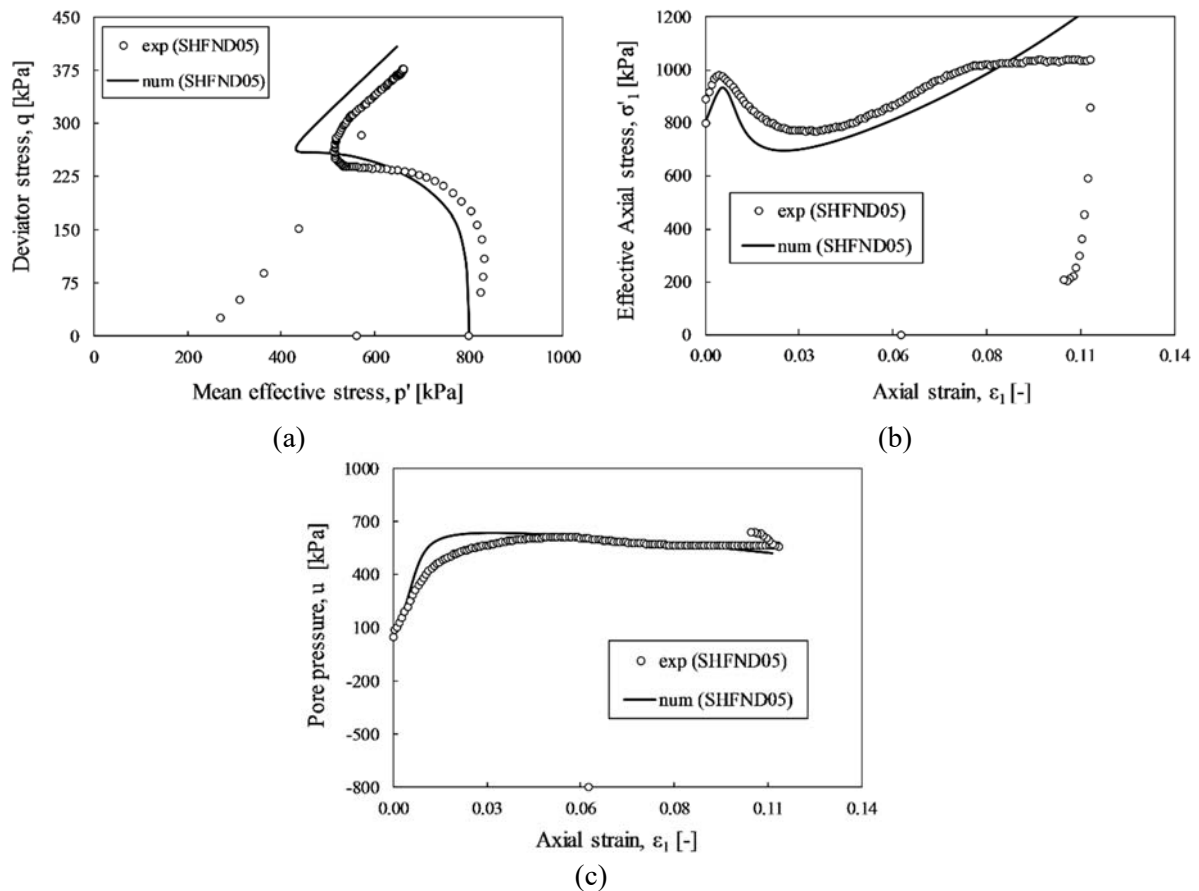


Figure 17: Biaxial test on loose Hostun sand ( $e_0=0.945$ ,  $p'_0=800$  kPa): (a) stress path, (b) deviatoric stress-stain response, (c) pore pressure build-up.

354

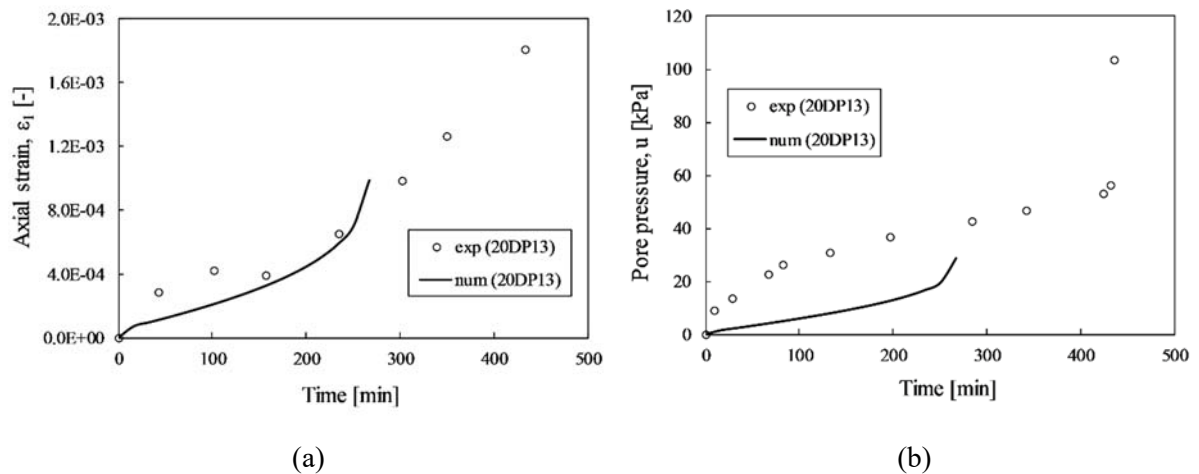


Figure 18: Undrained creep test on loose Hostun sand ( $e_0=0.900$ ,  $p'_0=100$  kPa): time evolution of (a) axial strain and (b) pore pressure.

355

356

## 5 CONCLUSIONS

357 An existing elasto-plastic model for sandy soils was reformulated as a Perzyna viscoplastic  
358 relationship to capture the rate-sensitive, pycnotropic and barotropic behaviour of sands under different  
359 loading/initial/boundary and drainage conditions. In particular, the suitability of two alternative viscous  
360 nucleus definitions, namely linear and exponential, was verified with respect to both creep and triaxial  
361 test data on Hostun sand from the literature. Importantly, the parameters governing the time-dependence  
362 of the material were separately calibrated against creep tests and then found suitable to reproduce the  
363 different loading paths/rates induced during standard triaxial tests. While the need for quite complex  
364 viscous nucleus functions was confirmed, it was also shown how challenging still is to unify the  
365 simulation of both drained and undrained responses under a single analytical formulation with a unique  
366 set of material parameters. Unlike most literature on the subject, this work highlights that simplistic  
367 assumptions about rate-sensitiveness may abruptly reduce the predictive potential of elasto-viscoplastic  
368 models.

369 From a modelling perspective, it should be noted that quantitative conclusions on the predictive range  
370 are very specific of both the viscous nucleus and yield functions adopted. The non-linearity needed of  
371 the viscous nucleus  $\Phi$  for good match with real data relates necessarily to how non-linear the  $f$  function  
372 is. When inherited from existing elasto-plastic formulations for granular soils, capped yield loci and  
373 plastic potentials are most often very non-linear, as necessary to capture the response under diverse  
374 loading programmes (including e.g. radial stress paths). This fact not only makes extension to  
375 viscoplasticity less straightforward, but also poses conceptual questions about the effects of convexity  
376 losses experienced by these functions in the overstress regime (i.e. outside the  $f=0/g=0$  loci). Expected  
377 consequences might concern the predicted stability of the constitutive response [23], a subject so far  
378 never explored from this standpoint. When documented, convexity-related issues might be remedied by  
379 resorting to recent convexification techniques ([73], [74]).

380 The discussion offered in this work also aimed to discourage simplistic use of viscoplasticity as a mere  
381 numerical expedient against mesh-dependence in strain-localisation problems. Conversely, the  
382 viscoplastic framework was reappraised as a physically sound approach to sand modelling, easy to  
383 extend to non-locality whenever also characteristic length effects are relevant.

384

## ACKNOWLEDGMENTS

385 The authors wish to thank the 7th Framework Programme of the European Union (ITN MuMoLaDe  
386 project 289911) and the University of Padova for financially supporting this work. The valuable input  
387 of Giuseppe Buscarnera and Constance Mihalache (Northwestern University) and Jacques Desrues  
388 (Université de Grenoble-Alpes) is also gratefully acknowledged.

389

390

## APPENDIX

391 *Stored energy function and hyperelastic behaviour*392 The strain energy function  $\psi(\boldsymbol{\varepsilon}^e)$  in Equation (5) is given by the following two-invariant expression:

$$\psi(\boldsymbol{\varepsilon}^e) = \bar{\psi}(\varepsilon_v^e, \varepsilon_s^e) = \tilde{\psi}(\varepsilon_v^e) + \frac{3}{2} \left[ G_0 + \frac{a}{\hat{k}} \tilde{\psi}(\varepsilon_v^e) \right] (\varepsilon_s^e)^2 \quad (20)$$

393 where:

$$\tilde{\psi}(\varepsilon_v^e) = \begin{cases} \hat{k} p_r \exp\left(\frac{\varepsilon_v^e}{\hat{k}} - 1\right), & \varepsilon_v^e \geq \hat{k} \text{ (or } p' \geq p_r) \\ p_r \varepsilon_v^e + \frac{p_r (\varepsilon_v^e - \hat{k})^2}{2\hat{k}}, & \varepsilon_v^e < \hat{k} \text{ (or } p' < p_r) \end{cases} \quad (21)$$

394 This model produces pressure-dependent bulk and shear elastic moduli.  $G_0, \hat{k}, a$  are constitutive  
 395 parameters,  $p_r$  is a reference mean effective stress, while  $\varepsilon_v^e, \varepsilon_s^e$  are the elastic volumetric strain and the  
 396 second invariant of the elastic strain deviator, respectively. When  $p' < p_r$  the hyperelastic law predicts a  
 397 linear elastic behaviour, whereas a fully non-linear pressure dependent behaviour is obtained for  $p' \geq p_r$ .  
 398 By taking the first and the second derivative of Equation (20) with respect to  $\boldsymbol{\varepsilon}^e$ , the following  
 399 expressions for the stress and the elastic stiffness tensor are obtained:

$$\boldsymbol{\sigma}' = \frac{\partial \psi(\boldsymbol{\varepsilon}^e)}{\partial \boldsymbol{\varepsilon}^e} = \left[ 1 + \frac{3a}{2\hat{k}} (\varepsilon_s^e)^2 \right] \theta_\varepsilon \mathbf{1} + 2 \left( G_0 + \frac{a}{\hat{k}} \tilde{\psi} \right) \mathbf{e}^e \quad (22)$$

400 and:

$$\mathbf{D}^e = \left[ 1 + \frac{3a}{2\hat{k}} (\varepsilon_s^e)^2 \right] K_\varepsilon \mathbf{1} \otimes \mathbf{1} + 2 \left( G_0 + \frac{a}{\hat{k}} \tilde{\psi} \right) \left[ \mathbf{I} - \frac{1}{3} \mathbf{1} \otimes \mathbf{1} \right] + 2 \left( \frac{a}{\hat{k}} \right) \theta_\varepsilon (\mathbf{1} \otimes \mathbf{e}^e + \mathbf{e}^e \otimes \mathbf{1}) \quad (23)$$

401 where,  $\mathbf{e}^e = \boldsymbol{\varepsilon}^e - \frac{1}{3} \text{tr}(\boldsymbol{\varepsilon}^e) \mathbf{1}$  is the deviatoric elastic strain and:

$$\theta_\varepsilon = \frac{\partial \tilde{\psi}(\varepsilon_v^e)}{\partial \varepsilon_v^e} = \begin{cases} p_r \exp\left(\frac{\varepsilon_v^e}{\hat{k}} - 1\right), & \varepsilon_v^e \geq \hat{k} \text{ (or } p' \geq p_r) \\ p_r \frac{\varepsilon_v^e}{\hat{k}}, & \varepsilon_v^e < \hat{k} \text{ (or } p' < p_r) \end{cases} \quad (24)$$

402

$$K_\varepsilon = \frac{\partial \theta_\varepsilon}{\partial \varepsilon^c} = \begin{cases} \frac{p_r}{\hat{k}} \exp\left(\frac{\varepsilon_v^c}{\hat{k}} - 1\right), & \varepsilon_v^c \geq \hat{k} \text{ (or } p' \geq p_r) \\ \frac{p_r}{\hat{k}}, & \varepsilon_v^c < \hat{k} \text{ (or } p' < p_r) \end{cases} \quad (25)$$

403

404

## REFERENCES

- 405 [1] di Prisco C, Imposimato S. Time dependent mechanical behaviour of loose sands. *Mechanics of*  
406 *Cohesive-Frictional Materials* 1996; **1**: 45–73.
- 407 [2] Lade PV, Yamamuro JA, Bopp PA. Influence of time effects on instability of granular materials,  
408 *Computers and Geotechnics* 1997; **20**(3-4):179–193.
- 409 [3] Tatsuoka F, Jardine RJ, Lo Presti D, Di Benedetto H, Kodaka, T. Characterising of the Pre-Failure  
410 Deformation Properties of Geomaterials. *Proceedings of the 14<sup>th</sup> International Conference on Soil*  
411 *Mechanics and Foundation Engineering*, Hamburg, Germany, 2129–2164, 1997.
- 412 [4] Di Benedetto H, Tatsuoka F. Small strain behavior of geomaterials: modelling of strain rate effects.  
413 *Soils and Foundations* 1997; **37**(2): 127–138.
- 414 [5] Di Benedetto H, Ibraim E, Cazacliu B. Time dependent behaviour of sand. *Proceedings of the 2<sup>nd</sup>*  
415 *International Symposium on Pre-failure Deformation Characteristics of Geomaterials*, Torino,  
416 Italy, Jamiolkowski M et al. (eds), 459–466, 1999.
- 417 [6] Di Benedetto H, Tatsuoka F, Lo Presti D, Sauzéat C, Geoffroy H. Time effects on the behaviour of  
418 geomaterials, *Deformation Characteristics of Geomaterials: Recent Investigations and Prospects*,  
419 Di Benedetto et al. (eds). Taylor & Francis Group, London, 59–123, 2005.
- 420 [7] Augustesen A, Liingaard M, Lade PV. Evaluation of Time-Dependent Behavior of Soils.  
421 *International Journal of Geomechanics* 2004; **4**(3):137–156.
- 422 [8] Pham Van Bang D, Di Benedetto H, Duttine A, Ezaoui A. Viscous behaviour of dry sand.  
423 *International Journal for Numerical and Analytical Methods in Geomechanics* 2007; **31**: 1631–  
424 1658.
- 425 [9] Perzyna P. The constitutive equations for rate sensitive plastic materials. *Quarterly of Applied*  
426 *Mathematics* 1963; **20**(4): 321–332.
- 427 [10] Duvaut G, Lion JL. *Les inequations en mécanique et en physique*. Dunod:Paris,1972.
- 428 [11] Wang WM, Sluys LJ, De Borst R. Viscoplasticity for instabilities due to strain softening and  
429 strain-rate softening. *International Journal for Numerical Methods in Engineering* 1997; **40** (20):  
430 3839–3864.
- 431 [12] Runesson K, Ristinmaa M, Mähler L. A comparison of viscoplasticity formats and algorithms.  
432 *Mech. Cohesive frictional Mater* 1999; **4**(1): 75–98.
- 433 [13] Carosio A, Willam K, Etse G. On the consistency of viscoplastic formulations. *International*  
434 *Journal of Solids and Structures* 2000; **37**(48–50): 7349–7369.

- 435 [14] Heeres O, Suiker A, de Borst R. A comparison between the Perzyna viscoplastic model and the  
436 Consistency viscoplastic model. *European Journal of Mechanics. A/Solids* 2002; **21**: 1–12.
- 437 [15] Di Benedetto H, Tatsuoka F, Ishihara M. Time-dependent shear deformation characteristics of  
438 sand and their constitutive modelling. *Soils and Foundations* 2002; **42**(2): 1–22.
- 439 [16] Tatsuoka F, Uchimura T, Hayano K, Koseki J, Di Benedetto H, Siddiquee MS. A. Time-  
440 dependent deformation characteristics of stiff geomaterials in engineering practice. In M.  
441 Jamiolkowski, R. Lancellotta, & D. Lo Presti (Eds.), *Pre-Failure Deformation Characteristics of*  
442 *Geomaterials*, 1161–1250, 1999.
- 443 [17] Perzyna P. Fundamental problems in viscoplasticity. *Advances in Applied Mechanics* 1966; **9**:  
444 243–377.
- 445 [18] Borja RI. *Modeling the monotonic and cyclic viscoplastic soil behavior. Proceedings of the*  
446 *second International Conference on recent advances in geotechnical earthquake engineering and*  
447 *soil dynamics* (ed. S. Prakash), vol 1.14: 37–40. Rolla, MO, USA: Missouri University of Science  
448 and Technology, 1991.
- 449 [19] di Prisco C, Imposimato S, Vardoulakis I. Mechanical modelling of drained creep triaxial tests on  
450 loose sand. *Géotechnique* 2000; **50**(1): 73–82.
- 451 [20] di Prisco C, Imposimato, S. Static liquefaction of a saturated loose sand stratum, *International*  
452 *Journal of Solids and Structures* 2002; **39**: 3523–3541.
- 453 [21] Yin ZY, Chang CS, Karstunen M, Hicher PY. An anisotropic elastic–viscoplastic model for soft  
454 clays. *International Journal of Solids and Structures* 2010; **5**: 665–677.
- 455 [22] Oka F, Adachi T, Yashima A. Instability of an elastoviscoplastic constitutive model for clay and  
456 strain localization. *Mechanics of Materials* 1994; **18**: 119–129.
- 457 [23] Pisanò F, di Prisco C. A stability criterion for elasto-viscoplastic constitutive relationships.  
458 *International Journal for Numerical and Analytical Methods in Geomechanics* 2015; **40**(1): 141–  
459 156.
- 460 [24] Marinelli F, Buscarnera G. Instability criteria for quasi-saturated viscous soils. *International*  
461 *Journal for Numerical and Analytical Methods in Geomechanics* 2017; DOI: 10.1002/nag.2746.
- 462 [25] Marinelli F, Pisanò F, di Prisco C, Buscarnera G. Model-based interpretation of undrained creep  
463 instability in loose sands. *Géotechnique* 2017; 1–14.
- 464 [26] Needleman A. Material rate dependence and mesh sensitivity on localization problems. *Computer*  
465 *Methods in Applied Mechanics and Engineering* 1988; **67**: 69–86.
- 466 [27] Loret B, Prevost JH. Dynamic strain localization in fluid-saturated porous media. *Journal of*  
467 *Engineering Mechanics* 1991; **117**(4):907–922.
- 468 [28] Sluys LJ. Wave propagation, localisation and dispersion in softening solids. *Ph.D. Thesis*, Delft  
469 University of Technology, 1992.
- 470 [29] Schrefler B A, Zhang HW, Sanavia L. Fluid-structure interaction in the localisation of Saturated  
471 porous media, *Zeitschrift für Angewandte Mathematik und Mechanik (Journal of Applied*  
472 *Mathematics and Mechanics, Z. Angew. Math. Mech.)* 1999; **79**(7): 481–484.
- 473 [30] Ehlers W, Graf T, Ammann M. Deformation and localization analysis of partially saturated soil.

- 474 *Computer Methods in Applied Mechanics and Engineering* 2004; **193**: 2885–2910.
- 475 [31] Rice JR. *The localisation of plastic deformation. Proceedings of the 14th IUTAM Congress,*  
476 *Koiter W.T. (ed.), Delft (North Holland, Amsterdam), 207–220, 1976.*
- 477 [32] di Prisco C, Imposimato S. Nonlocal numerical analyses of strain localization in dense sand.  
478 *Mathematical and Computer Modelling* 2003; **37**: 497–506.
- 479 [33] Lazari M, Sanavia L, Schrefler BA. Local and non-local elasto-viscoplasticity in strain  
480 localization analysis of multiphase geomaterials. *International Journal for Numerical and*  
481 *Analytical Methods in Geomechanics* 2015; **39**:1570–1592.
- 482 [34] Buscarnera G, Nova R. An elastoplastic strain hardening model for soil allowing for hydraulic  
483 bonding–debonding effects. *International Journal for Numerical and Analytical Methods in*  
484 *Geomechanics* 2009; **33**(8): 1055–1086.
- 485 [35] Jommi C. *Remarks on the constitutive modelling of unsaturated soils. Experimental Evidence and*  
486 *Theoretical Approaches in Unsaturated Soils, In Proceedings of an International Workshop,*  
487 *Trento, 139–153, 2000.*
- 488 [36] Jommi C, di Prisco C. A simple theoretical approach for modelling the mechanical behaviour of  
489 unsaturated soils (in Italian). *In Proceedings of the Conference “Il ruolo dei fluidi nei problemi*  
490 *di Ingegneria geotecnica”, 1: 167–188, 1994.*
- 491 [37] Nova R, Castellanza R, Tamagnini C. A constitutive model for bonded geomaterials subject to  
492 mechanical and/or chemical degradation. *International Journal for Numerical and Analytical*  
493 *Methods in Geomechanics* 2003; **27**: 705–732.
- 494 [38] di Prisco C, Imposimato S, Aifantis EC. A visco-plastic constitutive model for granular soils  
495 modified according to non-local and gradient approaches. *International Journal for Numerical*  
496 *and Analytical Methods in Geomechanics* 2002; **26**: 121–138.
- 497 [39] Schrefler BA. The finite element method in soil consolidation (with applications to surface  
498 subsidence), *PhD. Thesis, University College of Swansea, 1984.*
- 499 [40] Borja RI, Tamagnini C, Amorosi A. Coupling plasticity and energy-conserving elasticity models  
500 for clay. *Journal of Geotechnical and Geoenvironmental Engineering* 1997; **123**(10): 948–957.
- 501 [41] Tamagnini C, Castellanza R, Nova R. A generalized backward Euler algorithm for the numerical  
502 integration of an isotropic hardening elastoplastic model for mechanical and chemical degradation  
503 of bonded geomaterials. *International Journal for Numerical Methods in Engineering* 2002; **26**:  
504 963–1001.
- 505 [42] Lagioia R, Puzrin A, Potts D. A new versatile expression for yield e plastic potential surfaces.  
506 *Computers and Geotechnics* 1996; **19**(3): 171–191.
- 507 [43] Gudehus G. Elastoplastische stoffgleichungen für trockenen sand. *Ingenieur-Archiv* 1973; **42**:  
508 151–169.
- 509 [44] Pisanò F. Seismic Performance of Infinite Earth Slopes: Numerical Modelling, Constitutive Issues  
510 and Theoretical Considerations, *Ph.D. Thesis, Politecnico di Milano, Italy, 2011.*
- 511 [45] di Prisco C, Pastor M, Pisanò F. Shear wave propagation along infinite slopes: A theoretically  
512 based numerical study. *International Journal for Numerical and Analytical Methods in*  
513 *Geomechanics* 2012; **36**(5): 619-642.

- 514 [46] Uriel S. Intrinsic dynamic of the quasi-static mechanics of granular soils. *In Numerical Methods*  
515 *in Soil and Rock Mechanics*, Borm G, Meissner H (eds). Institut für Bodenmechanik und  
516 Felsmechanik der Universität Karlsruhe: Karlsruhe: 61–70, 1975.
- 517 [47] Been K, Jefferies MG. A state parameter for sands. *Géotechnique* 1985; **35**(2): 99–112.
- 518 [48] Wood DM, Belkheir K. Strain softening and state parameter for sand modelling. *Géotechnique*  
519 1994; **44**(2): 335–339.
- 520 [49] Manzari M, Dafalias Y. A critical state two-surface plasticity model for sands. *Géotechnique*  
521 1997; **47**(2): 255–272.
- 522 [50] Gajo A, Wood DM. Seven-Trent sand: a kinematic-hardening constitutive model: the q-p  
523 formulation. *Géotechnique* 1999; **49** (5): 595–614.
- 524 [51] Manzanal D, Fernández-Merodo JA, Pastor M. Generalized plasticity state parameter-based  
525 modelling of saturated and unsaturated soils. Part I: saturated state. *International Journal for*  
526 *Numerical and Analytical Methods in Geomechanics* 2011; **35**: 1347–1362.
- 527 [52] Lazari M. Finite element regularization for post localized bifurcation in variably saturated media,  
528 *Ph.D. Thesis*, University of Padova, Italy, 2016.
- 529 [53] Jirasék M. Objective modeling of strain localization. *Revue française de génie civil* 2002; **6**: 119–  
530 1132.
- 531 [54] Jirásek M, Rolshoven S. Comparison of integral-type nonlocal plasticity models for strain-  
532 softening materials. *International Journal of Engineering Science* 2003; **41**: 1553–1602.
- 533 [55] Lu X, Bardet JP, Huang M. Spectral analysis of nonlocal regularization in two-dimensional finite  
534 element models. *International Journal for Numerical and Analytical Methods in Geomechanics*  
535 2012; **36**: 219–235.
- 536 [56] di Prisco C, Stupazzini M, Zambelli C. Nonlinear SEM numerical analyses of dry dense sand  
537 specimens under rapid and dynamic loading. *International Journal for Numerical and Analytical*  
538 *Methods in Geomechanics* 2007; **31**(6): 757–788.
- 539 [57] Murianni A, Di Prisco C, Federico A. Numerical stability of non-local viscoplastic FEM analyses  
540 for the study of localisation processes. *Geomechanics and Geoengineering* 2013; **8**(4): 215–228.
- 541 [58] Lazari M, Sanavia L, Schrefler BA. Finite element modelling of shear bands in porous media by  
542 means of non-local viscoplasticity. *COMPLAS XIII: proceedings of the XIII International*  
543 *Conference on Computational Plasticity: fundamentals and applications*, Barcelona: CIMNE,  
544 2015, 140–150.
- 545 [59] Lewis RW, Schrefler BA. *The Finite Element Method in the Static and Dynamic Deformation*  
546 *and Consolidation of Porous Media*. John Wiley & Sons, Chichester, 1998.
- 547 [60] Gawin D, Schrefler BA. Thermo-hydro-mechanical analysis of partially saturated porous  
548 materials. *Engineering Computations* 1996; **13**(7): 113–143.
- 549 [61] Sanavia L, Pesavento F, Schrefler BA. Finite element analysis of non-isothermal multiphase  
550 geomaterials with application to strain localization simulation. *Computational Mechanics* 2006;  
551 **37**: 331–348.
- 552 [62] Sanavia L. Numerical Modelling of a Slope Stability Test by Means of Porous Media Mechanics.

- 553 *Engineering Computations* 2009; **26**(3), 245–266.
- 554 [63] Gawin D, Sanavia L. A unified approach to numerical modelling of fully and partially saturated  
555 porous materials by considering air dissolved in water. *Computer Modeling in Engineering and*  
556 *Sciences* 2009; **53**: 255–302.
- 557 [64] Gawin D, Sanavia L. Simulation of cavitation in water saturated porous media considering effects  
558 of dissolved air. *Transport in Porous Media* 2010; **81**: 141–160.
- 559 [65] Kakogiannou E, Sanavia L, Nicot F, Darve F, Schrefler BA. A porous media finite element  
560 approach for soil instability including the second-order work criterion, *Acta Geotechnica* 2016;  
561 **11**(4): 805–825.
- 562 [66] Cao TD, Sanavia L, Schrefler BA. A thermo-hydro-mechanical model for multiphase  
563 geomaterials in dynamics with application to strain localization simulation. *International Journal*  
564 *for Numerical Methods in Engineering* 2016; **107**(4): 312–337.
- 565 [67] Sheng D, Sloan SW, Gens A, Smith DW. Finite element formulation and algorithms for  
566 unsaturated soils. Part I: Theory. *International Journal for Numerical and Analytical Methods in*  
567 *Geomechanics* 2003; **27**(9): 745–765.
- 568 [68] Cattaneo F, Della Vecchia G, Jommi C. Evaluation of numerical stress-point algorithms on  
569 elastic–plastic models for unsaturated soils with hardening dependent on the degree of saturation.  
570 *Computers and Geotechnics* 2014; **55**: 404–415.
- 571 [69] Daouadji A, Al Gali H, Darve F, Zegloul A. Instability in Granular Materials: Experimental  
572 Evidence of Diffuse Mode of Failure for Loose Sands. *Journal of Engineering Mechanics* 2010;  
573 **136**(5): 575–588.
- 574 [70] Mokni M, Desrues J. Strain localisation measurements in undrained plane-strain biaxial tests on  
575 hostun RF sand. *Mechanics of Cohesive-Frictional Materials* 1998; **4**: 419–441.
- 576 [71] Alesani M, Fantini S. Stability analysis of the mechanical behaviour of granular materials under  
577 undrained conditions (in Italian). *Master Thesis*, Politecnico di Milano (Italy), 1998.
- 578 [72] Desrues J, Viggiani G. Strain localization in sand: an overview of the experimental results  
579 obtained in Grenoble using stereophotogrammetry. *International Journal for Numerical and*  
580 *Analytical Methods in Geomechanics* 2004; **28**: 279–321.
- 581 [73] Panteghini A, Lagioia R. An extended modified cam-clay yield surface for arbitrary meridional  
582 and deviatoric shapes retaining full convexity and double homothety. *Géotechnique* 2018; **68**(7):  
583 590–601.
- 584 [74] Panteghini A, Lagioia R. An approach for providing quasi-convexity to yield functions and a  
585 generalized implicit integration scheme for isotropic constitutive models based on 2 unknowns.  
586 *International Journal for Numerical and Analytical Methods in Geomechanics* 2018; **42**(6): 829–  
587 855.
- 588 [75] di Prisco C, Imposimato S, Nova R. Sand specimen undrained mechanical response to  
589 instantaneous load increments. *Proceedings of Plasticity'99, 7<sup>th</sup> International Symposium on*  
590 *plasticity and its current applications*, Cancun, Mexico, 557–560, 1999.
- 591

592

Table 1: List of constitutive parameters.

<i>Hyperelastic law</i>	
$\hat{k}$	slope of the swelling isotropic compression line
$a$	deviatoric-volumetric elastic coupling parameter
$G_0$	representative elastic shear modulus
$p_r$	reference pressure
<i>Yield function</i>	
$m_f$	yield function shape parameter
$\alpha_f$	yield function shape parameter
$M_{cf}$	stress obliquity for local yield locus maximum in triaxial compression
$M_{ef}$	stress obliquity for local yield locus minimum in triaxial extension
<i>Plastic potential</i>	
$m_g$	plastic potential shape parameter
$\alpha_g$	plastic potential shape parameter
$M_{cg}$	stress obliquity for isochoric plastic flow in triaxial compression
$M_{eg}$	stress obliquity for isochoric plastic flow in triaxial extension
<i>Hardening rule</i>	
$\rho_s$	mechanical hardening of pre-consolidation pressure
$\zeta_s$	dilatancy at failure
$r_{sw}$	hydraulic hardening of pre-consolidation pressure
<i>Viscous nucleus</i>	
$\gamma$	fluidity parameter
$\alpha$	viscous nucleus shape parameter

593

594

595

596

597

Table 2: Literature experimental tests on Hostun sand used for model calibration/validation.

Test name	Drainage	$p'_o$ [kPa]	$e_o$ [-]	Reference
Triaxial compression tests				
hos011	Drained	300	0.574	Gajo and Wood (1999) [50]
hos027	Drained	200	0.578	
hosfl10	Drained	300	0.800	
hosfl11	Drained	300	0.897	
d4	Drained	300	0.945	
hosfl14	Drained	50	0.838	
hflw10	Drained	600	0.822	
batr02	Undrained	200	0.940	

batr06	Undrained	200	0.830	
alert9	Undrained	200	0.666	
400.95_li	Drained	400	0.950	Pham Van Bang et al. (2007) [8]
CD-1	Drained	100	1.052	
CD-2	Drained	300	0.954	
CD-3	Drained	750	1.010	Daouadji et al. (2010) [69]
ICU-1	Undrained	100	1.086	
ICU-2	Undrained	300	1.060	
ICU-3	Undrained	750	1.083	
<b>Biaxial compression test</b>				
SHFND05	Undrained	800	0.945	Mokni and Desrues (1998) [70]
<b>Creep tests</b>				
T100a	Drained	100	0.950	di Prisco and Imposimato (1996) [1]
80.71_ci	Drained	80	0.710	Pham Van Bang et al. (2007) [8]
20DP13	Undrained	100	0.900	Alesani and Fantini (1998) [71]

598

599

Table 3:  $D_r$ -insensitive constitutive parameters.

Elastic law	Yield locus	Plastic potential
$a=0.0$	$\alpha_f=0.99$	$\alpha_g=0.24$
$k=0.0046$	$m_f=1.10$	$m_g=1.10$
$p_r=1$ kPa	$M_{ef}=0.52$	$M_{cg}=1.28$
	$M_{ef}=0.44$	$M_{eg}=1.0$

600

601

Table 4:  $D_r$ -dependent constitutive parameters.

Sample Density	$G_0$ [kPa]	$\rho_s$ [-]	$\zeta_s$ [-]	$r_{sw}$ [-]
Loose	14000	111	0.00	5.45
Dense	45000	2000	0.480	0.32
Limit void ratios	$e_{max}$	1.041	$e_{min}$	0.58

602

603

Table 5: Viscous parameters for loose Hostun sand (from drained creep tests).

Viscous nucleus	$\gamma$ [ $s^{-1}$ ]	$\alpha$ [-]
linear	$4 \cdot 10^{-9}$	1.0
exponential	$2 \cdot 10^{-14}$	28.90

604

605

606

Table 6: Viscous parameters for dense Hostun sand (from drained creep tests).

Viscous nucleus	$\gamma$ [ $s^{-1}$ ]	$\alpha$ [-]
linear	$1 \cdot 10^{-8}$	1.0
exponential	$2 \cdot 10^{-10}$	28.90

607

608

609

Table 7: Viscous parameters for undrained conditions (exponential viscous nucleus).

Sample density	$\gamma$ [ $s^{-1}$ ]	$\alpha$ [-]
TXU - Loose	$2 \cdot 10^{-5}$	28.90
TXU - Dense	$2 \cdot 10^{-4}$	28.90

610